BAYERO JOURNAL OF PHYSICS AND MATHEMATICAL SCIENCES

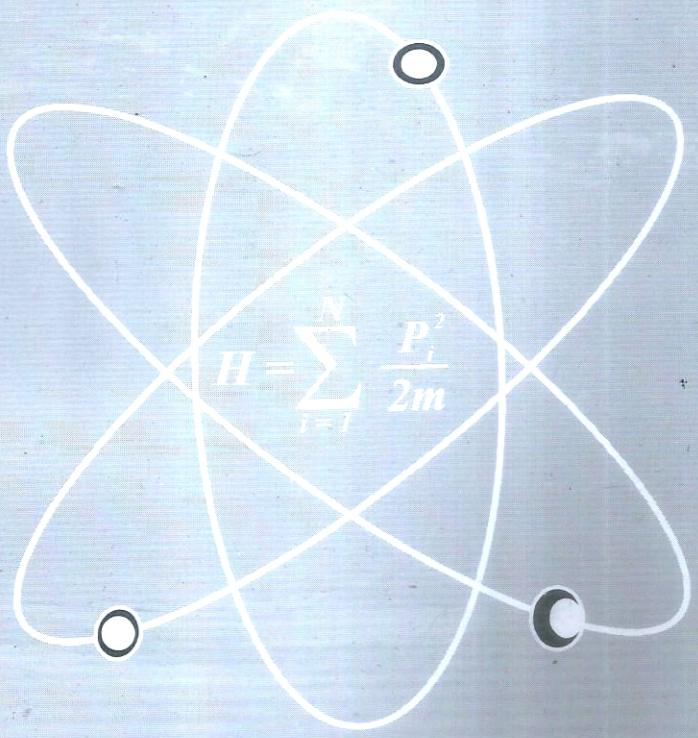

VOLUME 9, No. 1
JULY, 2018.

Published by:
THE DEPARTMENTS OF PHYSICS AND
MATHEMATICAL SCIENCES, BAYERO UNIVERSITY, KANO.

MEMBERS OF THE EDITORIAL BOARD

TABLE OF CONTENTS

Preparation of Microspherical Flowerlike $Ni(Oh)_2$/Graphene Oxide Electrode for Electrochemical Capacitor Application
Khaleed, A. A., Igumbor, E. and Omotoso, E. 1 – 8

Parabolic Trough Solar Collector: Development and Performance Evaluation Using Selected Absorber Coatings
Yunusa, A. and Abusafiyan, A. 9 – 15

Electronic Transport Properties of Vinazene Molecular Device for Photovoltaic Applications By Dft-Negf Approach
Lawal, A. Ebea Moses, A. and Gidado, A. S. 16 – 24

Physicochemical Analysis of Water Samples of Selected Borehole from some Local Government in Kano, Kano State, Nigeria.
Auwalu, S., Usman, Y. K., Lawan, I. and Farouq, S. M. 25 – 34

Design and Construction of Microcontroller Based Automatic Car Parking System.
Galadanci, G. S. M. and Galadima, B. Y. 35 – 48

Total Reaction Cross Section and One-Nucleon Removal Cross Section of ^{37}Mg from $^{37}Mg + {}^{12}C \rightarrow {}^{12}C + {}^{36}Mg + {}^{1}n$ Reaction System in the Glauber Theorem
Adamu, I. D. and Sa'adu, I. 49 – 54

Calculation of Reactions Cross-Section by Particles Induced Nuclear Reactions
Ahmad, I., Koki, F. S., and Ibrahim, Y. Y. 55 – 63

First Principle Study of Thermodynamic and Optical Properties of Tm^{3+} Interstitial in Germanium, Using Hybrid Functional (HSE06).
Igumbor, E., Khaleed, A. A. and Omotoso, E. 64 – 68

Evaluation of Air Pollutants and the Effect of its Transport and Mixing Processes on Air Quality: A Case Study of Selected Industries in Kano State - Nigeria.
Idris, M., Darma, T. H., Koki, F. S. and Said, R. S. 69 – 78

Synthesis, Structural and Electrical Properties of Nanocrystalline Barium Titanate Ceramic Using Mechanochemical Method.
Muazu, A., Ahmadu, U., Umar, S., Amoka, A. 79 – 88

Theoretical Analysis of the Exponentiated Generalized U-Quadratic Distribution
Muhammad, M., Rano, S. A., Sani, R. I. and Musa, S. A. 89 – 100

Spotlighting the Geophysical Modeling
Saleh, M. 101 – 108

Electronicstructure Properties Analysis of Zinc Oxide Nanosheets Attached to in Electrodes.
Yusuf, S., Tarauni, Y. U., Abdullahi, S. S., Muhammad, A., Ali, M. U., Aliyu, A. and Jamo, H. U. 109 – 118

Application of Electrical Resistivity Method for Investigation of Competence of Building Foundation at the Permanent Site of Yusuf Maitama Sule University Kano, Nigeria.
Yusuf, S. and Aku, M. O. 119 – 126

A Review on a Study of Farm and Soil Pollution Using Magnetic Susceptibility Method
Zira, A. M., Lawal, A. A. and Sule, P. 127 – 135

Magnetic Susceptibility of Irrigation Farm Soil as a Proxy for Pollution Study
Aminu, A. L., Sule P. and Zira, A. M. 136 – 144

Single Crystal Silicon Solar Cells – A Review
Musa, A. O. and Yunusa, A. 145 – 153

Structural Performance of Bismuth Oxide Doped Zinc Silicate (Willemite) Glass Ceramics from Waste Material
Auwalu, I. A., Jamo, U. H., Diso, D. G., Aminu, A., Inuwa, A. F., Alhassan, M. and Umar, S. A. 154 – 159

Enhancing Mechanical Properties of Porcelain Body By Substituting Quartz by RHA at Different Mould Pressures
Jamo, U. H., Abdu, S., Ibrahim, K. L., Muhammad, A., and Yusuf, H. 160 – 168

Geomagnetic Evaluation of the Basement Structure at the Permanent Site of Federal University Lokoja, Kogi State
Gani, L. I., Ibrahim, A. and Rabba, J. A. 169 – 178

Evaluation of Essential and Toxic Elements in Date Palm Fruits around Zaria area using Atomic Absorption Spectrometry
Onoja, M. A., Kassimu, A. A., David, D. and Umar, J. L. 179 – 183

First Principles Study of Electronic, Elastic and Optical Properties of Bi_2Te_3 under Pressure
Lawal, A., Kona, A. M. and Madugu, M. L. 184 – 197

Model Predictive Control Design For Magnetic Suspension System
Gaya, M.S., Abdulkadir, R. A., Muhammad, A., Saleh, M. A., Umar, I. D. and Imam, K. A. 198 – 202

Evaluation of Excitation Function for the Productions of Polonium-207 and Polonium-208 Isotopes from Bismuth-208 Nucleus
Ahmad, I. 203 – 209

Impedance and Modulus Spectroscopy Studies on Lead Free Ba $(Ti_{0.96}Sn_{0.02}Zr_{0.02})O_3$ Ceramics
Muazu, A., Ahmadu, U., Halim, A., Umar, S. and Amoka, A. 210 – 224

Neutron Removal Cross Section From Elastic and Inelastic Breakup Processes of ^{11}Be From $^{11}Be + {}^{12}C \rightarrow {}^{12}C + {}^{10}Be + {}^{1}n$ Reaction System
Adamu, I. D. and Sa'adu, I. 225 – 230

Magnetic Properties of Nano-structured CoCrTa thin films
Gana, U. M. 231 – 235

Remanence Properties of Nano-structured CoCrTa thin films
Gana, U. M. 236 – 240

Spectral Analysis of High Aeromagnetic Data Over Kabo. (Sheet Number 80), Kano State, Nigeria
Suleiman, A., Aku, M. O. and Sanusi, Y. A. 241 – 248

Analysis of Heavy Metals Accumulation and Sources / Origin in Fish (Tilapia) Organs using Statistical Tools
Isa, N. F., Haladu, B., Tijjani, B. I. and Ibrahim, M. U. 249 – 256

BAJOPMAS JOURNAL 9(1): 210 – 226
Printed in Bayero University, Kano - Nigeria.

IMPEDANCE AND MODULUS SPECTROSCOPY STUDIES ON LEAD FREE Ba ($Ti_{0.96}Sn_{0.02}Zr_{0.02}$) O_3 Ceramics

Muazu, A.[1*], Ahmadu, U.[2], Halim, A.[3], Umar, S.[4] and Amoka, A.[4],
[1*]Department of Physics, Federal college of Education (T), Bichi, Kano, Nigeria.
[2.] Department of Physics, Federal University of Technology, Minna, Nigeria.
[3] Department of Physics, Universiti Putra Malaysia, Serdang, Malaysia.
[4] Department of Physics, Ahmadu Bello University, Zaria, Nigeria.
Corresponding author: Tel: +2318033216484, e-mail: hasumm@yahoo.com

ABSTRACT
The electrical parameters of the polycrystalline sample of Ba ($Ti_{0.96}Sn_{0.02}Zr_{0.02}$) O_3 in a frequency range of 40 Hz to 1MHz at 200-400°C were obtained by the AC complex impedance spectroscopy technique. A single phase perovskite compound of tetragonal symmetry with space group P4mm was confirmed by X-ray diffraction technique. This study was carried out by means of simultaneous analysis of impedance, modulus and electrical conductivity. Impedance spectroscopy analysis reveal a non-Debye type relaxation phenomenon. Grain and grain boundary conduction is observed from complex impedance spectrum by the appearance of two semicircular arcs in the Cole-Cole (Nyquist) plot at 400°C. This suggests that the grains and grain boundaries are responsible for the conduction mechanism of the material at high temperature. The bulk resistance of the material decreases with rising temperature similar to a semiconductor which indicates the negative temperature coefficient of resistance (NTCR) character of the sample which makes it for use as highly sensitive thermistor. The bulk and grain boundary resistance, capacitance and relaxation time at 400°C are found to be 44.07, 148.41 kΩ, 3.23×10^{-10}, 1.71×10^{-8} Farad, and 1.42×10^{-5}, 2.55×10^{-3} respectively. AC conductivity of the ceramics increases as a function of frequency due to relaxation phenomenon arisen due to mobile charge carriers. The nature of frequency dependence of AC conductivity confirms the Jonscher's power law.

Keywords: X-ray diffraction, electrical impedance, modulus, conductivity.

1.0 Introduction
Barium titanate (BT) compounds are the best-known perovskite ferroelectric compounds. They are extensively studied [1, 2] due to their peculiarity to accommodate different types of dopants. The electrical and dielectric properties of BT can be modified using various type of dopants as well as processing procedures. This opened gates for doped nanosized barium titanate materials for specific technological applications, such as capacitors, sensors with positive temperature coefficients of resistivity, piezo-electric transducers and ferroelectric thin-film memories. Among the dopants Ba (Zr_xTi_{1-x}) O_3 (BZT) has been chosen in the fabrications of ceramic capacitors because Zr^{4+} is chemically more stable than Ti^{4+} [3]. Moreover, Zr-substitution at Ti-site has been found to be an effective way to decrease the Curie temperature and exhibited several interesting features in the dielectric behavior of $BaTiO_3$ ceramics. Also doped BT compositions, Ba ($Ti_{1-x}Sn_x$) O3 (BST) system has drawn wide attention due to their manifestation of diffuse-type phase transition [4-6]. It is known that Curie temperature of barium titanate system can be altered by the substitution of dopants into either A- or B-site. Distortion in TiO_6 octahedra, due to B site doping leads to diffused phase transition. Partial replacement of titanium by tin, zirconium, or hafnium generally leads to a reduction in Tc and an increase in the permittivity maximum (ε max)

with dopant content [7]. In all ferroelectrics, in general, the study of electrical conductivity is very important to realize the associated physical properties and nature of conductivity in these materials, and it is well known that the interior defects such as A-site vacancies, space charge electrons or oxygen vacancies have great influence on ferroelectric fatigue or ionic conductivity of the material [8-11]. Considering that the solid defects play a decisive role in all of these applications, it is very important to gain a fundamental understanding of their conductive mechanism. Various kinds of defects are always suggested as being responsible for the dielectric relaxations at high temperature range.

Complex impedance spectroscopy is a nondestructive method [12] to distinguish the grain boundary and grain-electrode effects, which usually are the sites of a trap for oxygen vacancies and other defects. It is also useful in establishing space charge polarization and its relaxation mechanism, by appropriately attributing different values of resistance and capacitance to the grain and grain boundary effects. It appears naturally in complex plane in the form of succession semicircles representing electrical phenomenon involved in the polycrystalline material due to grain, grain boundaries, electrical interface effect and correlate between the dielectric and electrical characteristics [13-15].Therefore, the contributions to the overall electrical property by various components in the material are separated out easily. Impedance spectroscopy measurement studies for other materials [16, 17] were also used to gain an insight into electrical mechanism inside those materials.

The complex electrical modulus formalism has been used in the analysis of the electrical properties because it gives the primary response of the bulk of the sample, eliminating the effects due to electrode/ electrical contacts. Thus, it is particularly suitable for extracting information due to the electrodes and determining conductivity relaxation times [18]. The combined usage of both the impedance and modulus spectroscopy is that Z'' plots highlight the phenomenon of largest resistance and M'' plots pick up those of smallest capacitance [19]. In this paper the structural, microstructural and conduction behavior of nanocrystalline Ba $(Ti_{0.96}Sn_{0.02}Zr_{0.02})$ O_3 is reported using impedance spectroscopy and electric modulus analysis.

1.1 Theoretical Background

Impedance properties arise due to intragrain, intergrain and electrode processes. The motion of charges could occur in a variety of ways, namely charge displacement (long-range or short-range), dipole re-orientation, space charge formation etc. The frequency dependent properties of a material can be described as complex permittivity (ε^*), complex impedance (Z^*), complex admittance (Y^*), complex electric modulus (M^*) and dielectric loss or dissipation factor (tan δ). The real (ε', Z', Y', M') and imaginary ($\varepsilon'', Z'', Y'', M''$) parts of the complex parameters are in turn related to one another as follows:

$$\varepsilon^* = \varepsilon' + j\varepsilon'' \quad (1)$$

$$Z^* = Z' + jZ'' = \frac{1}{jC_o\varepsilon^*\omega} \quad (2)$$

$$Y^* = Y' + jY'' = jC_o\varepsilon^*\omega \quad (3)$$

$$M^* = M' + jM'' = j\varepsilon_o Z^*\omega \quad (4)$$

$$\tan\delta = \frac{\varepsilon''}{\varepsilon'} = \frac{M'}{M''} = \frac{Y'}{Y''} = \frac{Z'}{Z''} \quad (5)$$

where $\omega = 2\pi f$ is the angular frequency, C_o is the free geometrical capacitance, and $j^2 = -1$.

These relations offer wide scope for a graphical analysis of the various parameters under different conditions of temperature or frequency. The useful separation of intergranular phenomena depends ultimately on the choice of an appropriate equivalent circuit to represent the sample properties.

2.0 Experimental procedures

2.1 Synthesis of Zirconium and tin co-doped Barium titanate

Ba $(Ti_{0.96}Sn_{0.02}Zr_{0.02})O_3$ nanocrystalline powders were synthesized by a combination of solid-state reaction and high energy ball milling technique (HBM).The startisng materials were analytical grade of oxide precursors, $BaCO_3$ (≥ 99%, Merck, Germany), TiO_2 (99.9%, Aldrich, U.S.A), ZrO_2 (99%, Strem, U.S.A and SnO_2 (99.9%, Strem, U.S.A). Stoichiometric amounts of the oxides were weighed according to the nominal composition and ball-milled for 12 h in alcohol .The mixture was dried in an oven and calcined in an alumina crucible at 1050°C for 4 h in air to yield Ba $(Ti_{0.96}Sn_{0.02}Zr_{0.02})O_3$ ceramic via the following reaction:

$$BaCO_3 + (0.96)\ TiO_2 + (0.02)\ SnO_2 + (0.02)\ ZrO_2 \longrightarrow Ba\ (Ti_{0.96}Sn_{0.02}Zr_{0.02})\ O_3 + CO_2$$

The calcined powders were ball milled in an isopropyl alcohol as wetting medium using SPEX 8000 Mixer/Mills. They are functionally described as shaker mills or high-energy ball mills, the Mixer/Mills shake containers back and forth approximately 1080 cycles per minute (60 Hz model) and was performed at room temperature for 7 hours. The milling was stopped for 15 min after every 60 minutes of milling to cool down the system. The slurry was put in an oven and dried at 90°C for 24 hrs. The milled powder was compacted at 49033.25 N/m^2 to make pellets of size 10 mm in diameter and 1 mm thickness using polyvinyl alcohol (PVA) as a binder. The pellets were sintered in a programmable furnace at temperatures of 1190°C for 2 hr. in alumina crucibles.

Phase identification of calcined and sintered powders was identified using X-ray diffractometer (XPERT-PRO) with monochromatic Cu Kα radiation at λ = 1·54178 Å at 40 kV/40 mA in the 2θ range from 20° to 80° with scan step time of 19.44 s and scan step size of 0.033° in continuous scan mode. The experimental density of the sample was calculated using Archimedes principle. The morphological studies of the sintered sample were carried out by using field emission scanning electron microscopy (FESEM, JEOL 7600F, U. S. A), operated at a voltage of 15 kV and images captured at 5 kV with magnification of ×100,000. In order to measure the dielectric properties, silver paste was painted on the polished sample as the electrodes and fired at 550°C for 15 min. The dielectric properties of the ceramic were evaluated using Impedance Analyzer (Agilent 4294A, Japan) at an oscillation amplitude of 500 mV in the frequency and temperature range of 40 Hz – 1M Hz and 30 to 400°C respectively.

The prepared sample is:

Table 1. Samples description

Sample	Description
BTSZ	Ba $(Ti_{0.96}Sn_{0.02}Zr_{0.02})\ O_3$

3.0 Results and discussions

3.1 Phase analysis and microstructure

The XRD pattern (Figure 1a) shows the room temperature of Ba $(Ti_{0.96}Sn_{0.02}Zr_{0.02})\ O_3$ ceramic sintered at 1190°C for 2 hr. It is seen that the composition is of single phase perovskite structure without any trace of a secondary phase containing Zr and Sn. The presence of sharp and well defined diffraction peaks indicate that this ceramic material has a degree of crystallinity at a long range which implies that Sn^{+4} and Zr^{+4} have entered the unit cell maintaining the perovskite structure in the solid solution. The enlarged XRD patterns (Figure 1b) of the Ba $(Ti_{0.96}Sn_{0.02}Zr_{0.02})\ O_3$ ceramics in the range of 2θ from 44.75 to 45.75° clearly shows that the crystal structure is tetragonal with the splitting of the (200) and (002) characteristic peaks at 2θ of 45.25° and is in agreement with the joint committee on powder diffraction standards (JCPDS file no. 98-000-2020). From the *hkl* values and XRD data cell dimensions were calculated: a = 4.0019 Å, *b* = 4.0019 Å, *c* =

4.02107Å and α = β = γ = 90°.Thus, the analysis confirmed that this crystal belongs to the tetragonal perovskite system. The average crystallite size t of the ceramic sample was calculated from the full width at half maximum of the (110) diffraction peaks using Scherrer formula [21]:

$$t = \frac{k\lambda}{\beta cos\theta}, \quad (6)$$

where k = 0.9 is the crystalline shape factor, λ is the X-ray wavelength, β is the full width at half maximum (FWHM) and θ is the Bragg angle in radian corresponding to the peak. The values of crystallite size obtained from XRD data and crystal cell volumes for Ba $(Ti_{0.96}Sn_{0.02}Zr_{0.02})$ O_3 ceramics were found to be 42.7 nm and 64.398 $Å^3$ respectively.

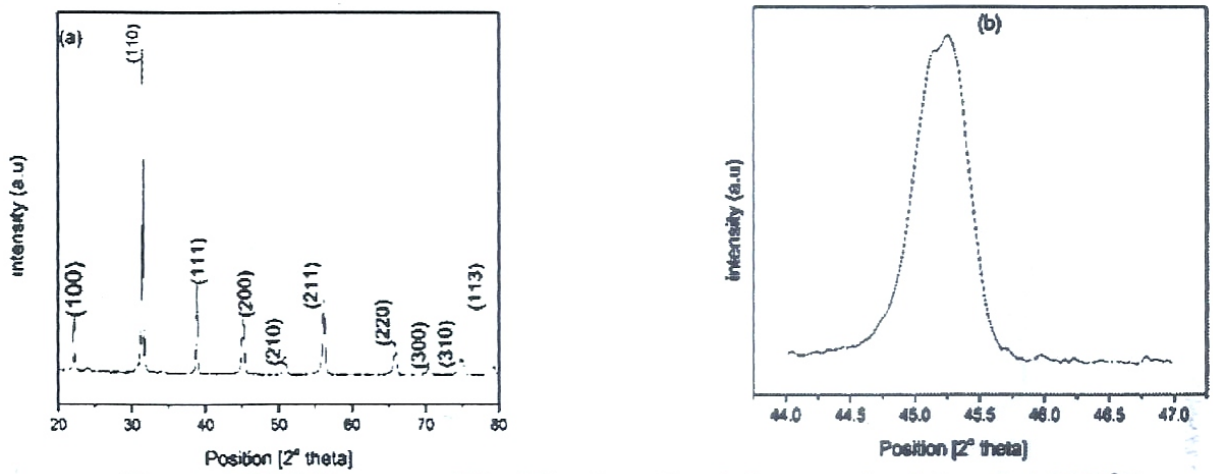

Figure 1. XRD Patterns of Ba $(Ti_{0.96}Sn_{0.02}Zr_{0.02})$ O_3 ceramic sintered at 1190°C

Figure 2 shows the typical FESEM micrographs of BT, BTSZ1, BTSZ2 and BTSZ3 ceramics sintered at 1190°C for 2 hrs. It can be seen that all the sintered ceramic samples are dense and have varying microstructures with presence of voids. The presence of voids in the FESEM images indicates that the pellets have certain amount of porosity. The grain size and grain boundary are observed very clearly in the non-agglomerated region and the average grain size determined by using intercept technique is 199.65 nm. This large grain size of Ba $(Ti_{0.96}Sn_{0.02}Zr_{0.02})$ O_3 ceramics result as the ionic radii of Zr^{+4} (0.72 Å) and Sn^{+4} (0.69 Å) is greater than that of Ti^{+4} (0.61 Å) which can induce lattice strain in the unit cell volume and grain size which indicates that Zr can promote the growth of BTSZ based grains in the ceramics.

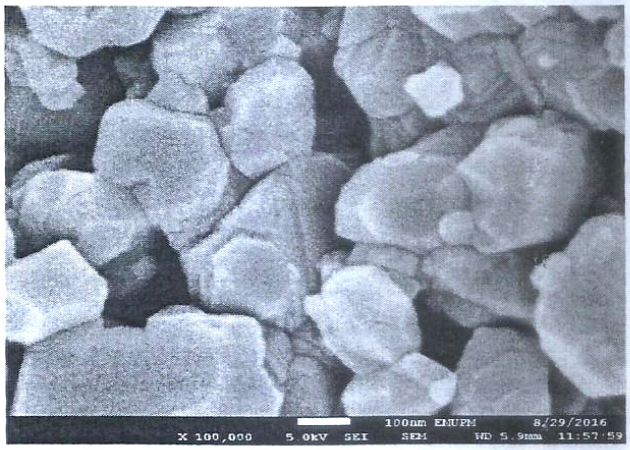

Figure 2. FESEM images of Nano crystalline of Ba $(Ti_{0.96}Sn_{0.02}Zr_{0.02})$ O_3 samples at magnification of × 200,000 sintered at 1190°C.

3.2. Dielectric measurements

3.2.1 Frequency dependent of dielectric constant

The variation of real (ε'), imaginary (ε'') dielectric constant and tangent loss (tan δ) at room temperature for Ba ($Ti_{0.96}Sn_{0.02}Zr_{0.02}$) O_3 as a function of frequency from 40 Hz to 1 MHz range at 30 to 150°C is shown in Figure 3(a). It can be seen that the value of dielectric constant is higher at lower frequency and decreases with increasing frequency due to the dielectric relaxation, which is a characteristic feature of the ferroelectric materials irrespective of composition of the specimens [22]. In Figure 3(b) there is strong dispersion of ε'' at low frequency which deceases with increasing frequency and temperature. Beyond 10^4 Hz, ε'' starts to increases with increasing frequency and temperature with the appearance of peaks at $>10^5$. The peaks shift towards higher frequency with increase of temperature, this is evidence of the presence of relaxation in the system. The dielectric constant response of a system is due to electronic, ionic, dipole and space charge polarizations, among others. Again at low frequencies, all types of polarization contributes and as the frequency is increased, polarizations with large relaxation times cease to respond and hence the decrease in ε' [23]. At lower frequencies, ε' is maximum because the contributions from the space charge polarization are large, which reduces slowly with the increase in frequency. The space charge polarization arises by the accumulation of charges at the grain boundaries and at the electrode interface. At higher frequencies, contributions from the polarizations having high relaxation time cease resulting in the decrease in ε' [24].

It's known that the tangent loss in ferroelectrics is due to a combination of space charge polarization and domain wall relaxation [25]. In Figure 3(c), the increase of tan δ beyond 10^4 and 10^5 Hz at all the temperature is due to extrinsic loss phenomena which indicate diffuse nature of phase transition [26].

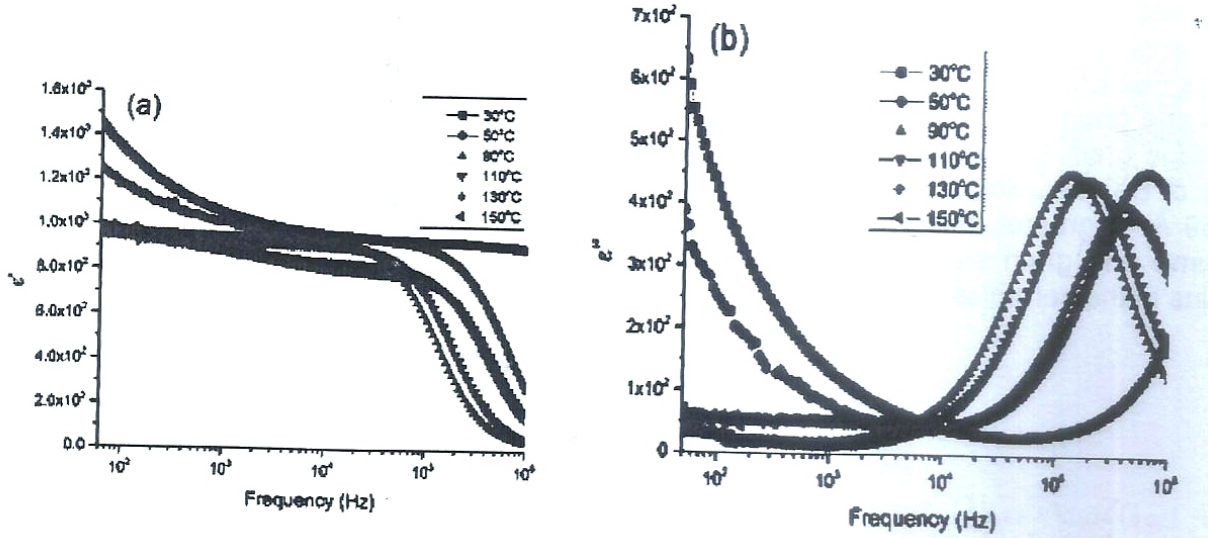

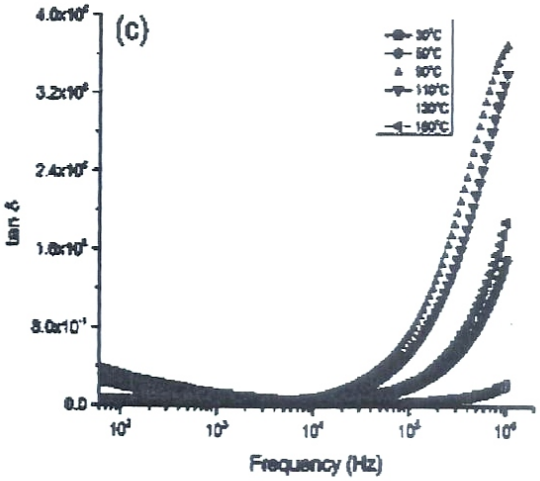

Figure 3. Variation of frequency dependence of (a) real (b) imaginary dielectric constant (c) tangent loss of Ba ($Ti_{0.96}Sn_{0.02}Zr_{0.02}$) O_3 ceramic sintered at 1190°C.

3.2.2 Temperature dependence of dielectric constant and tangent loss

The variation of dielectric constant and tangent loss as a function of temperature of Ba ($Ti_{0.96}Sn_{0.02}Zr_{0.02}$) O_3 ceramic measured from room temperature to 150°C at the different frequencies is shown in Figure 4. It is clear that the dielectric constant of Ba ($Ti_{0.96}Sn_{0.02}Zr_{0.02}$) O_3 ceramic is at room temperature which decreases with increasing temperature and is less than the one obtain in CuO-modified Ba ($Ti_{0.96}Sn_{0.02}Zr_{0.02}$) O_3 ceramics synthesized using solid state method [27]. The sample does not manifest any sign of a phase transition implying that its *Tc* may be below room temperature. The shifting of transition temperature (Tc) to a lower value can be explained by the larger radius of Zr^{+4} (0.72 Å) and Sn^{+4} (0.69 Å). Compared to Ti^{+4} (0.60 Å) and the fact that Sn^{4+} occupies sites formerly occupied by Ti^{4+}. Also, the non-ferroelectric barium stannate dilutes the ferroelectricity of barium titanate and thus makes the spontaneous polarization less stable. The result is that the phase transition temperature of Ba ($Ti_{0.96}Sn_{0.02}Zr_{0.02}$) O_3 ceramics shifts progressively towards a lower temperature. Uchino et al. (1984) suggested that with decreasing grain size, Tc was shifted downward through room temperature, eventually tending toward 0K at some critical particle size [28]. The decrease of dielectric constant of samples sintered by HBM should be attributed to two factors, grain size in nanometer range and distortion of crystal lattice caused by HBM. As the grain boundaries increases the grain size decrease and the grain boundary exhibited low-permittivity, which means the polarization of grain boundary may be little or even none. That causes the dielectric constant to decrease as the grain size decreases. The dielectric loss of Ba ($Ti_{0.96}Sn_{0.02}Zr_{0.02}$) O_3, BTSZ2 and BTSZ3 ceramics is shown in Figure 4. The dielectric loss of Ba ($Ti_{0.96}Sn_{0.02}Zr_{0.02}$) O_3 samples is higher at room temperature which decreases with increase of temperature and beyond 70°C it becomes almost independent of doping concentration and temperature. The loss tangent of Ba ($Ti_{0.96}Sn_{0.02}Zr_{0.02}$) O_3 ceramics decreases with increasing Zr content because of the fact that, the chemical stability of Zr4+ is preferable to that of Ti [29].

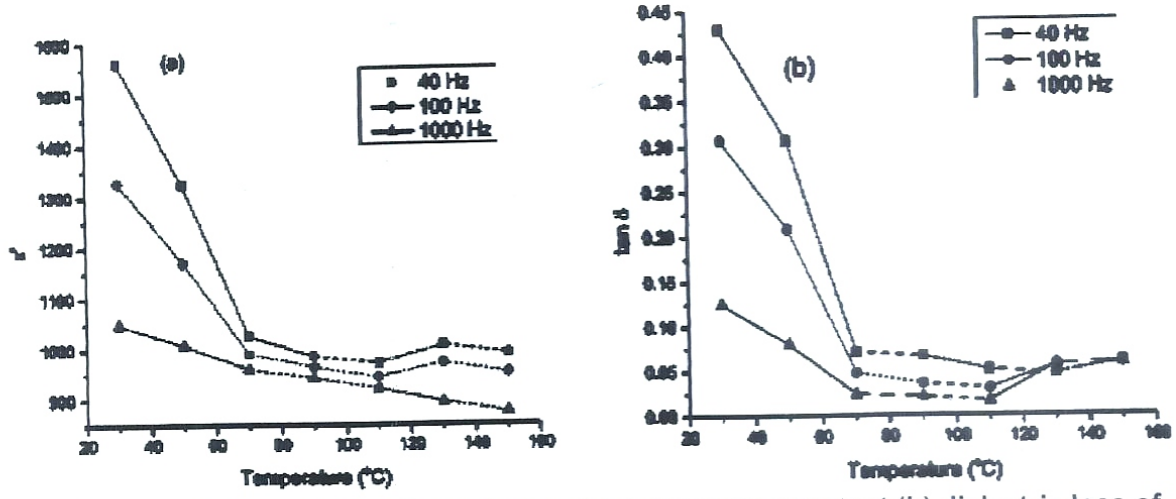

Figure 4. Temperature dependence of (a) dielectric constant (b) dielectric loss of nanocrystalline Ba ($Ti_{0.96}Sn_{0.02}Zr_{0.02}$) O_3 ceramics measured at different frequencies.

3.3 Complex impedance spectroscopy analysis

Figure 5 shows the variation of the real (Z') and imaginary (Z'') parts of impedance with frequency at 200 to 400°C. It is observed that the magnitude of Z'decreases with the increase in frequency for different measured temperatures. This indicates an increase in the ac conductivity with the increase in frequency. Similar behavior was found in the variation of Z'' with frequency (Figure 5(b)).The coincidence of Z' and Z'' values at higher frequencies at all temperatures indicates a possible release of space charge [30] and a consequent lowering of the barrier properties in the material [31]. Further, at low frequencies the Z'' values decrease with the rise in temperature, i.e. show negative temperature coefficient of resistance (NTCR) behavior similar to semiconductors [32].

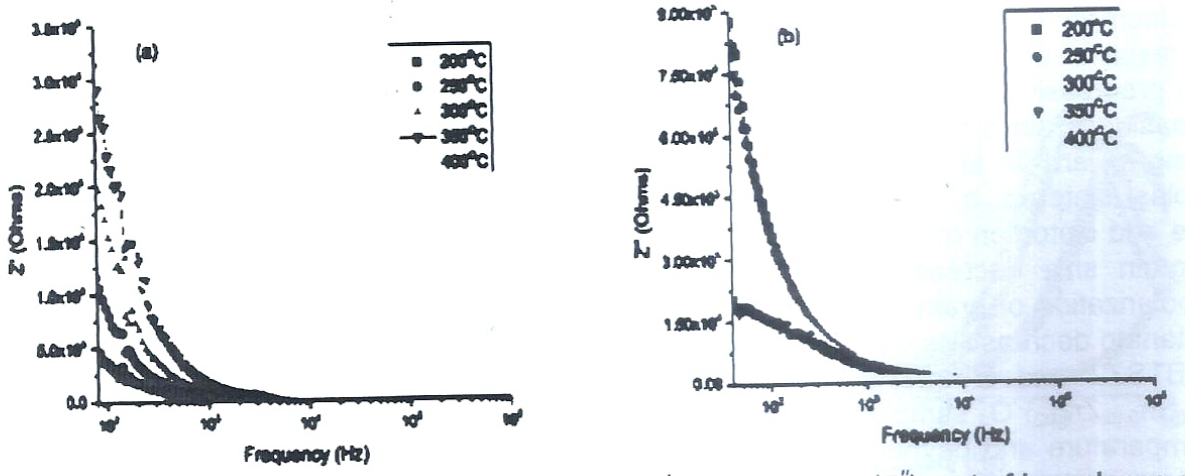

Figure 5. Frequency dependences of (a) real (Z') (b) imaginary (Z'') part of impedance of nanocrystalline Ba ($Ti_{0.96}Sn_{0.02}Zr_{0.02}$) O_3 samples at 30 to 150°C. The inset shows the corresponding dielectric loss plots at 200 to 400°C.

Figure 6(a)–(e) shows the complex impedance plots (Z^*) or Cole–Cole plots, i.e. plotting imaginary part Z''against the real part Z' of complex impedance $Z^* = Z' + jZ''$of Ba ($Ti_{0.96}Sn_{0.02}Zr_{0.02}$) O_3 ceramics, performed at 200, 250, 300, 350 and 400°C over a wide frequency range (40 Hz–1 MHz). The observed data was modeled on an equivalent circuit having series combination of two parallel resistor–capacitor elements (shown in the inset of

Figure 6(e)) [33, 34]. The real (Z') and imaginary (Z'') parts of total impedance of the equivalent circuit are defined as

$$Z' = \frac{R_g}{1+(\omega R_g C_g)^2} + \frac{R_{gb}}{1+(\omega R_{gb} C_{gb})^2} \quad (7.0)$$

$$Z'' = R_g\left[\frac{\omega R_g C_g}{1+(\omega R_g C_g)^2}\right] + R_{gb}\left[\frac{\omega R_{gb} C_{gb}}{1+(\omega R_{gb} C_{gb})^2}\right] \quad (8.0)$$

where R_g and C_g are the grain resistance and grain capacitance, R_{gb} and C_{gb} are the grain boundary resistance and grain boundary capacitance at the interfacial region respectively and ω is the angular frequency. The two semicircles in Figure 6(e) represent two types of relaxations that correspond to the grain (high-frequency range) and grain boundary (low-frequency range).

Intercept of semicircles on the Z'axis give the grain resistance R_g in high frequency range and grain boundary resistance (R_{gb}) in low frequency range.

It was observed that with the increase in temperature the slope of the lines decreases and the curve move towards real (Z') axis indicating the increase in conductivity of the sample. At high temperatures (200 - 350°C), the partially formed arc due to grains (bulk) are visible and with increasing temperature 400°C two semicircles are formed (Figure 4e) representing resistance for grain (R_g) and grain boundary (R_{gb}) effect in the material. Hence, grain and grain boundary effects could be separated at these temperatures. The high-frequency semicircle corresponds to a bulk contribution, and the low frequency semicircle corresponds to the grain boundary effect [35]. It was also observed that with the increase in temperature the radius of the semicircles decreases representing decrement in the resistivity. The value of bulk resistance (R_g) and grain boundary resistance (R_{gb}) obtained from the intercepts of the semicircular arcs formed at 400°C on the real axis (Z') are 44.08 and 148.4 kΩ respectively. These plots exhibit depressed semicircles having canters lying below the real axis confirming the presence of non-Debye type of relaxation phenomenon in the materials [36]. The samples resistance was found to decrease with rising temperature which suggests a negative temperature coefficient of resistance (NTCR) and indicating a typical semiconducting behavior of Ba ($Ti_{0.96}Sn_{0.02}Zr_{0.02}$) O_3 ceramic.

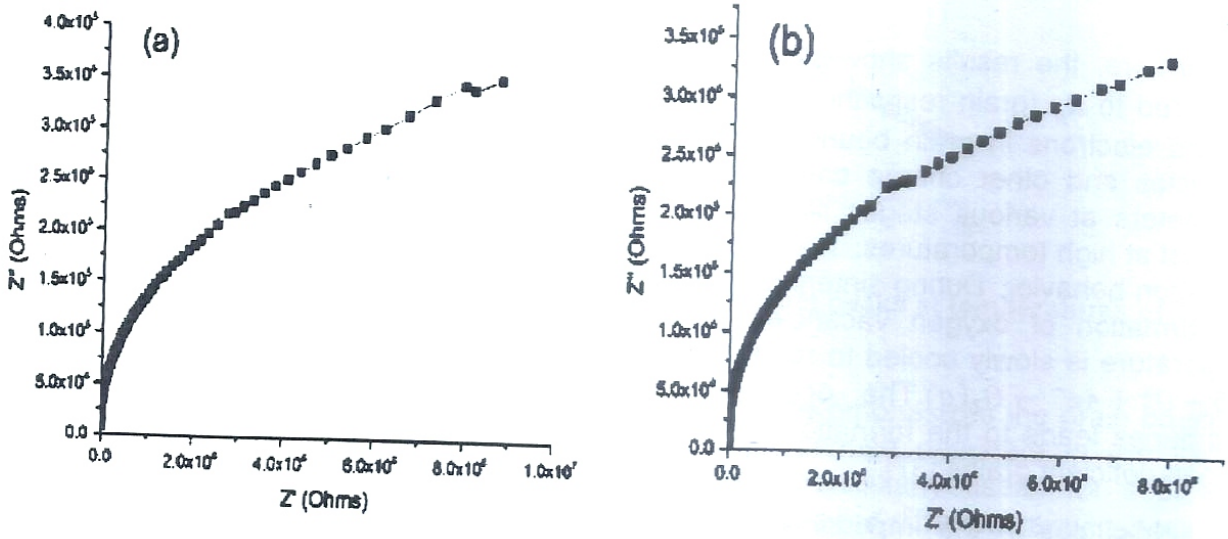

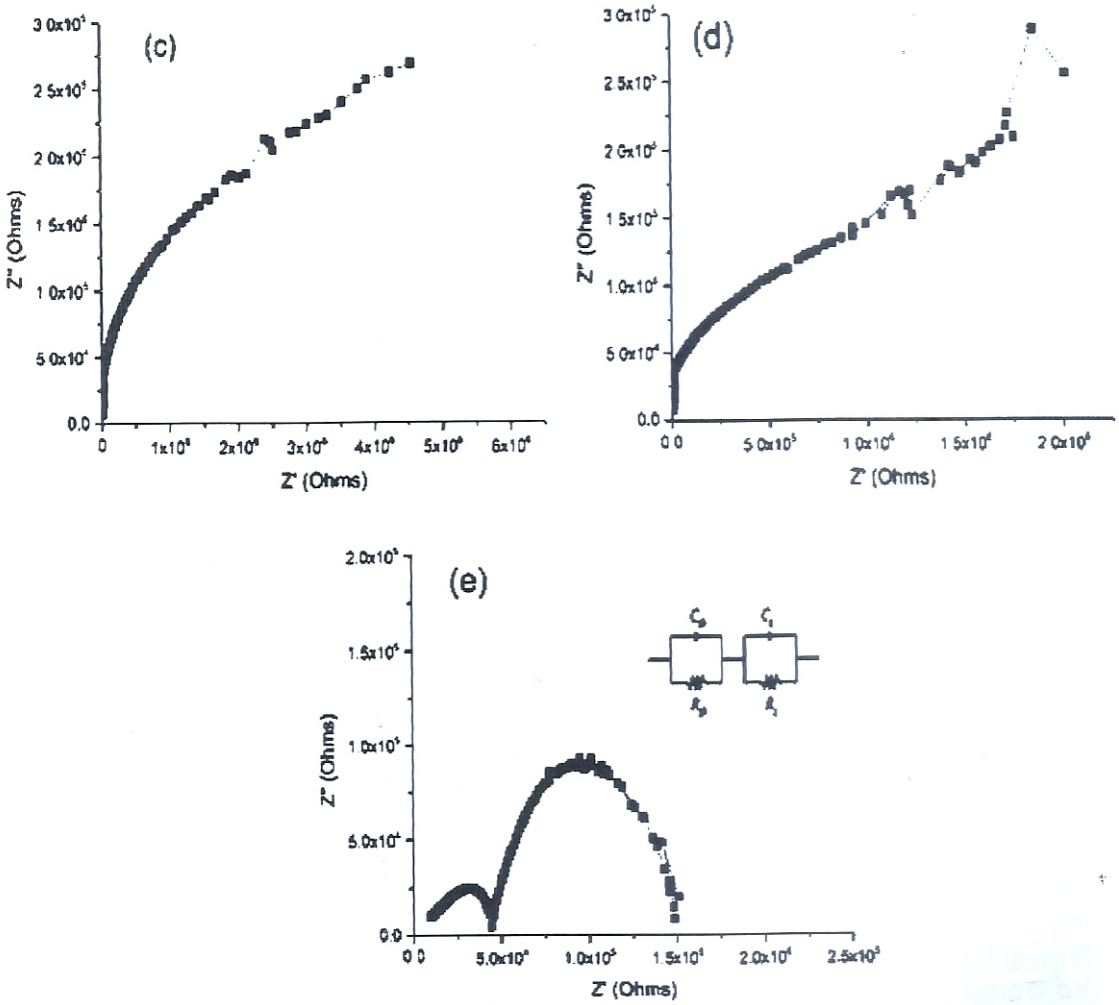

Figure 6. The plot of $Z^{'}$versus $Z^{''}$ (Nyquist or Cole-Cole plots) for nanocrystalline Ba ($Ti_{0.96}Sn_{0.02}Zr_{0.02}$) O_3 (a) 200°C (b) 250°C (c) 300°C (d) 350°C (e) 400°C taken over a wide frequency range of 40 Hz to 1MHz.

Furthermore, the results showed a higher value of R_{gb} (grain boundary resistance) as compared to R_g (grain resistance) due to a lower concentration of oxygen vacancies and trapped electrons in grain boundaries. This can be explained as the creation of oxygen vacancies and other charge carriers (e.g., electrons and holes) are related to process parameters at various stages like calcination and sintering during the synthesis of the material at high temperatures. These defects greatly influence the conduction and dielectric relaxation behavior. During sintering at high temperature, oxygen loss increases leading to the formation of oxygen vacancies as $2O_o^x \rightarrow O_2(g) + 2V\ddot{o} + 4e^-$. However, when the temperature is slowly cooled to room temperature in air, a re-oxidation process occurs as $2V\ddot{o} + O_o^x + 4e^- \rightarrow O_2(g)$.The occurrence of this re-oxidation process at the grain boundaries leads to the formation of an insulating grain boundary and highly conductive oxygen deficient grains [37].

The semicircles in the impedance spectrum have a characteristic peak occurring at a unique relaxation frequency ($\omega_r = 2\pi f$). It can be expressed as: $\omega_r\ RC = \omega_r\tau = 1$, with the resonance frequency as;

$$f_r = \frac{1}{2\pi\tau} = \frac{1}{2\pi RC} \qquad (9)$$

where τ is relaxation time. The respective capacitances (C_g and C_{gb}) due to the grain and grain boundary effects can be calculated using this relation. The values of R_g, R_{gb}, C_b and C_{gb} obtained from Cole-Cole plots at different temperatures are listed in Table 2. The relaxation time due to both the bulk and grain boundary effect (τ_g and τ_{gb}) has been calculated using Eq. (7).

Table 2:

Sample	Temp °C	R_g (Ω)	R_{gb} (Ω)	C_g(Farad)	C_{gb}(Farad)	τ_g(10^{-5})	τ_{gb} (10^{-3})
BTSZ	400	44077.3	148405.04	3.23E-10	1.71E-08	1.42	2.55

Figure 7 shows the normalized Z''behavior with frequency. Two distinct peaks at low and high frequencies were observed. The lower frequency peak is due to the relaxation of the space charges associated with the oxygen vacancies at the grain boundary layers, whereas the higher frequency peak is attributed to oxygen vacancies relaxation inside the grains. At lower frequency, a pronounced relaxation process can be seen due to bounding of the space charges by the grain boundary. However, with increasing frequency, the space charge polarization is reduced as it becomes easier for them to relax and recombine with the vacancies in grain interiors. In addition, a broadening of the peak due to spread of relaxation times in the ceramic was also evident. These relaxation processes are due to the presence of immobile species at low temperature and associated defects (oxygen vacancies) in the ceramic at higher temperature.

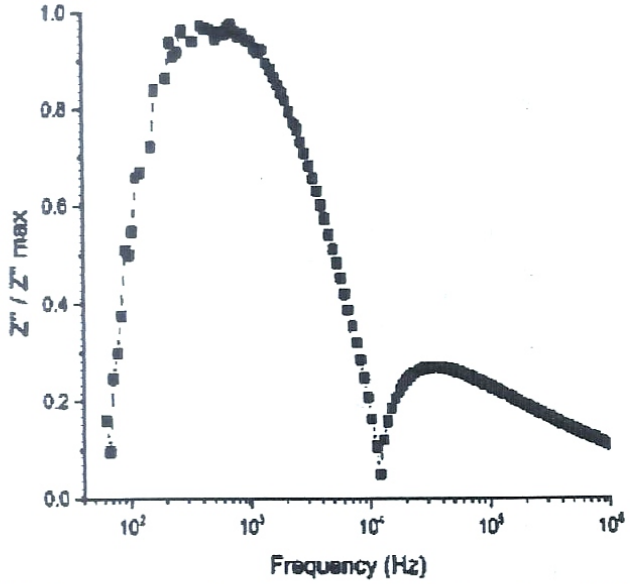

Figure 7. Normalized Z with frequency showing two distinct peaks at temperatures of 400°C.

3.4 Complex dielectric modulus analysis

In polycrystalline materials, the modulus of the impedance emphasizes the grain boundary conduction process, while bulk effects on frequency domain dominate in the electric modulus formalism. Modulus spectroscopy plots are particularly useful for separating spectral components of materials having similar resistances but different capacitances. The other advantage of the electric modulus formalism is that the electrode effect is suppressed. Modulus analysis is an alternative approach to explore electrical properties of the material and magnify any other effects present in the sample as a result of different relaxation time

constants. The values of real (M') and imaginary (M'') components of the modulus are obtained from the following expressions:

$$M' = \omega C_o Z' \quad (10)$$

$$M'' = \omega C_o Z'' \quad (11)$$

where C_o is the geometrical capacitance of the empty cell.

The complex modulus spectrum (M' versus M'') is shown in Figure 8. It indicates the electrical phenomenon with the smallest capacitance occurring in a dielectric system [38]. The appearance of a single arc in the spectrum confirms the single phase characteristic of the ceramics. Moreover, the asymmetric semicircular arc confirms the presence of electrical relaxation phenomena in the material [39]. It is clear that the modulus plane shows five semicircles for temperatures, the intercept of the semicircles with the real axis indicates the total capacitance contributed by the grain. The modulus spectrum shows a marked change in its shape upon increasing temperature, suggesting a change in the value of capacitance of the material with temperature.

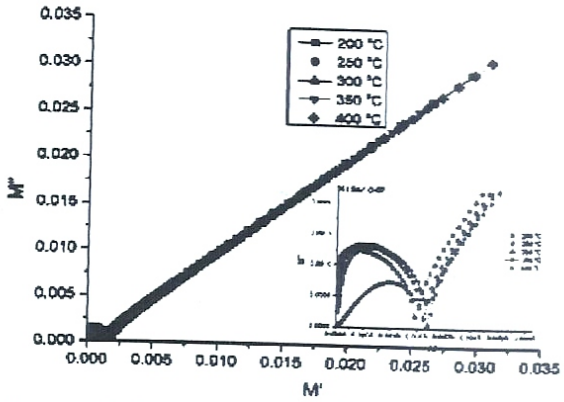

Figure 8. The complex modulus spectrum (M'versus M'') for Ba ($Ti_{0.96}Sn_{0.02}Zr_{0.02}$) O_3 at different measuring temperatures. Inset shows exploded plots at 200 to 400°C.

Figure 9 shows the variation of real (M') and imaginary (M'') parts of the electrical modulus in the frequency range of 40 Hz-1 MHz at 200 to 400°C. It is characterized by a very low value (almost zero) of M' in the low-frequency region followed a continuous increase with increasing frequency, having a tendency to saturate at a maximum asymptotic value in the high-frequency region at all the measuring temperatures. This can be attributed to the presence of conduction phenomena due to short-range mobility of charge carriers [40]. Figure 9(b) exhibits that the maxima of the imaginary component of modulus (M''max) shifts towards higher relaxation frequency with rising temperature. This behavior suggests that the dielectric relaxation is thermally activated in which hopping mechanism of charge carriers dominates intrinsically [41]. The asymmetric broadening of the peak indicates the spread of relaxation with different time constant, and hence the relaxation in the material is of non-Debye type.

The scaling behavior of the sample was studied by plotting normalized parameters (i.e., M/M''max vs, log (f /$fmax$), $fmax$ is the frequency corresponding to max M'') at various temperatures. The coincidence of all the curves/peaks of different temperatures into a single curve/peak indicates temperature independent dynamic processes occurring in the material [42]. The region where the peak occurs is an indication mobility with the increase in frequency [40] .This curve provides us with information about dielectric processes occurring in the material and the magnitude of mismatch between the peaks.

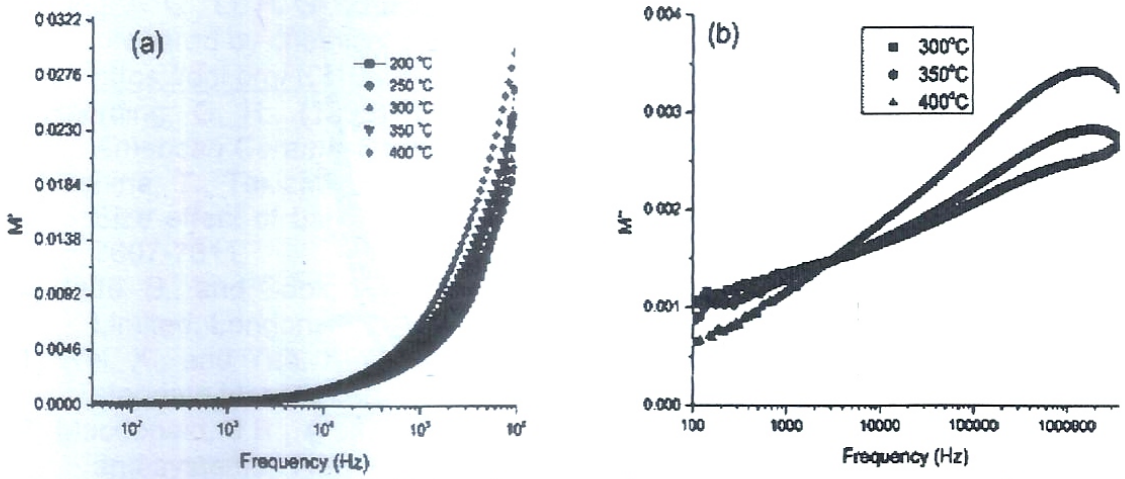

Figure 9. Variations of (a) real part of M' and (b) imaginary part of M'' for the Ba $(Ti_{0.96}Sn_{0.02}Zr_{0.02})\ O_3$ ceramic with frequency at different temperatures.

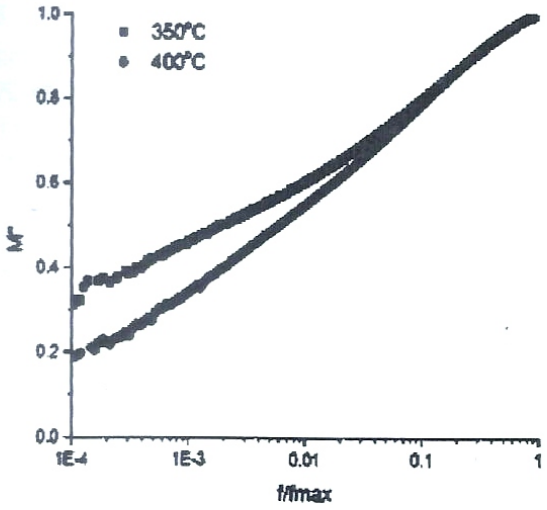

Figure 10. Modulus scaling behavior of (*M"/M"max*) versus log (*f/fmax*)

3.5 A.C. conductivity analysis

The temperature–frequency dependence of electrical conductivity can be represented by an equation proposed by Jonscher [43]:

$$\sigma_{ac} = \sigma_{dc} + A\omega^n \qquad (12)$$

where σ_{dc} conductivity is due to the excitation of electrons from a localized state to the conduction band, and $A\omega^n$ is the ac conductivity which consists of all dispersion phenomena. A is the frequency independent constant and n an exponent, $0 < n < 1$; both of these terms are temperature dependent. Figure 11 shows frequency dependence AC plots of Ba $(Ti_{0.96}Sn_{0.02}Zr_{0.02})\ O_3$ ceramic for various temperatures. AC conductivity of the samples were calculated from the impedance data, using the formula

$$\sigma_{ac} = \frac{t}{AZ'} \qquad (13)$$

At low frequency AC conductivity remained constant at lower frequencies and increased rapidly at higher frequencies and increased with increasing temperature at all frequencies as already reported [44], which is generally known as hopping frequency and which may be attributed to the increase in the number of charge carriers and their drifted mobility which are thermally activated [45].

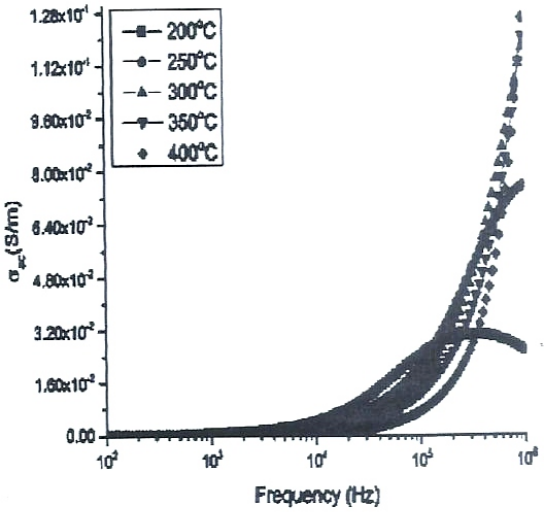

Figure 11. Dependence of σ_{ac} of Ba ($Ti_{0.96}Sn_{0.02}Zr_{0.02}$) O_3 ceramic on frequency

4.0 Conclusion

Nanocrystalline Ba ($Ti_{0.96}Sn_{0.02}Zr_{0.02}$) O_3 ceramic, synthesized by mechanochemical method, was found to have single phase perovskite tetragonal structure at room temperature. The FESEM images of powders show that the grains are irregular in shape and the average grain size is found to be 199.65 nm with large specific area and slightly agglomerated. The temperature and frequency dependence of the dielectric permittivity, impedance and electric modulus in Ba ($Ti_{0.96}Sn_{0.02}Zr_{0.02}$) O_3 have been performed. The temperature dependent dielectric study reveals that the phase transition has shifted towards lower temperature values with increasing Sn substitution. Complex impedance Cole–Cole plots of impedance in Ba ($Ti_{0.96}Sn_{0.02}Zr_{0.02}$) O_3 ceramic suggests the relaxation to be non-Debye-type. Cole–Cole plots show both grain and grain boundary contributions to impedance at 400°C. The compositions exhibited an NTCR behavior for the fabrication of highly sensitive thermistor. Frequency dependence of ac conductivity analysis shows that ac resistance follows the universal power law, as suggested by Jonscher. The conduction mechanism of the material may be due to the hopping of charge carriers. Thus, the prepared lead-free Ba ($Ti_{0.96}Sn_{0.02}Zr_{0.02}$) O_3 ceramics will use for MLCC and thermistors application.

References

[1] A. Mishra, N. Mishra (2012). "Iron-doped $BaTiO_3$: Influence of iron on physical properties", *International Journal of Material Science and Application.* 1, 14–21

[2] Kumar, M. M., Suresh, M.B., Surya, S.V., Kumar, G. S. and Bhimasankaram, T. (1998). Dielectric relaxation in $Ba_{0.96}Bi_{0.04}Ti_{0.96}Fe_{0.04}O_3$. *J. Appl. Phys.,* 84, 6811–6814.

[3] Cheng, B. L., Wang, C., Wang, S.Y., Lu, H., Zhou, Y.L., Chen, Z.H. and Yang, G.Z. (2005). Dielectric properties of ($Ba_{0.8}Sr_{0.2}$) (Zr_xTi_{1-x}) O3 thin films grown by pulsed-laser deposition, *J. Eur. Ceram. Soc.* 25, 2295–2298.

[4] Xiaoyong, W., Yujun, F. and Xi, Y. (2003). Dielectric relaxation behavior in barium stannate titanate ferroelectric ceramics with diffused phase transition *Appl. Phys. Lett.* 83, 2031, doi: 10.1063/1.1609037

[5] Lu, S.G., Xu, Z.K. and Chen, H. (2004). Tunability and relaxor properties of ferroelectric barium stannate titanate ceramics, *Appl. Phys. Lett.* 85, 5319, https://doi.org/10.1063/1.1829794

[6] Wei, X., and Yao, X. (2007). Preparation, structure and dielectric property of barium stannate titanate ceramics, *Mater. Sci. Eng.* B 137,184-188

[7] Jiang, A. Q., Li, H. G., Zhang, L. D. (1998). Dielectric study in nanocrystalline $Bi_4Ti_3O_{12}$ prepared by chemical coprecipitation, *J. Appl. Phys.* 83, 4878, https://doi.org/10.1063/1.367287

[8] Haertling, G. H., (1999). Ferroelectric ceramics: history and technology. *Journal of American Ceramic Society*, 82 (4): 797-818.

[9] Hoshina, T., Takizawa, K., Li, J., Kasama, T., Kakemoto H., and Tsurumi, T. (2008). Size effect of barium titanate: fine particles and ceramics, *Jpn. J. Appl. Phys.,* 47, 7607-7611

[10] Jaffe, B., and Cook, W R., Jaffe, H. (1971). Piezoelectric ceramics, Academic Press Limited, London,

[11] Wei, X., and Yao, X. (2007). Preparation, structure and dielectric property of barium stannate titanate ceramics, *Mater. Sci. Eng.* B 137,184-188

[12] Macdonald, J.R., (1987). Ed. Impedance spectroscopy--Emphasizing solid materials and systems. New York: Wiley-Interscience

[13] Bidault, O., Goux, P., Kchikech, M., Belkaoumi, M., Maglione, M. (1994). Space-charge relaxation in perovskites, *Phys. Rev. B*, 49, 7868. DOI: 10.1103/PhysRevB.49.7868.

[14] Li, Y.J., Chen, X. M., Hou, R. Z., Tang, Y. H., (2006). Maxwell–Wagner characterization of dielectric relaxation in $Ni_{0.8}Zn_{0.2}Fe_2O_4/Sr_{0.5}Ba_{0.5}Nb_2O_6$ composite. *Solid State Commun.* 137 (3), 120-125. DOI:10.1016/j.ssc.2005.11.017.

[15] Khan, M. H., Pal, S., Bose, E. (2013). Room temperature frequency-dependent complex impedance and conductivity behavior of $BaTiO_3$–$La_{0.7}Ca_{0.3}MnO_3$ composites. *Can. J. Phys.,* 91(12): 1029-1033. DOI: 10.1139/cjp-2012-0509

[16] Ahmadu, U., Tomas, Ŝ., Jonah, S. A., Musa, A. O. Rabiu, N. (2013). Equivalent circuit models and analysis of impedance spectra of solid electrolyte $Na_{0.25}Li_{0.75}Zr_2(PO_4)_3$. *Adv. Mat. Lett.* 4(3), 185-195

[17] Wu, Y., Nguyen, C., Seraji, S., Forbess, M.J., Limmer, S.J., Chou, T., and Cao, G. (2001). Processing and Properties of Strontium Bismuth Vanadate Niobate Ferroelectric Ceramics *Journal of the American Ceramic Society*. 84: 2882-2888.

[18]Rao, K. S., Krishna, P.M., Prasad, D.M., Latha, T.S. and Satyanarayana, C. (2008). Low frequency dielectric dispersion studies in ferroelectric ceramics of $Pb_{0.77}K_{0.26}Li_{0.2}Ti_{0.25}Nb_{1.8}O_6$. *Indian J Eng Mater. Sci 15*(2):*215*–223.

[19] Jacob, R., Harikrishnan Nair, G., Isac, J. (2015). Impedance spectroscopy and dielectric studies of nanocrystalline iron Doped barium strontium titanate ceramics. *Processing and Application of Ceramics,* 9(2): 73–79

[20] Hannachi, N. I. Chaabane, K. Guidara, A. Bulou, F. H. (2010). AC electrical properties and dielectric relaxation of $[N(C_3H_7)_4]_2Cd_2Cl_6$, single crystal. *Mater. Sci. Eng.* B 172, 24-32

[21] Sambasiva, K. Rao, D. Madhava Prasad, P. Murali Krishna, B. Tilak, K. C. Varadarajulu, (2006). Impedance and modulus spectroscopy studies on $Ba_{0.1}Sr_{0.81}La_{0.06}Bi_2Nb_2O_9$ ceramic. *Mater. Sci. Engg.* B 133(1-3), 141-150.

[22] Scherrer, P., Gottinger Nachirichten. (1918). 2, 98-100

[24] Chopra, S., Sharma, S., Goel, T.C., Mendiratta, R.G. (2004). Effect of Annealing temperature on the Microstructure of chemically deposited Ca modified Lead Titanate Effect thin films. *Appl. Sur. Sci.* pp. 230-207.

[25] Sarabjit, S., Thakur, O.P., Chandra, P. and Raina, K.K. (2005). Structural and electrical properties of lanthanum-substituted lead titanate ceramics. *Phase Transitions* 78,655

[26] Wu, Y., Nguyen, C., Seraji, S., Forbess, M.J., Limmer, S.J., Chou, T. and Cao, G. (2001). Processing and Properties of Strontium Bismuth Vanadate Niobate Ferroelectric Ceramics. *Journal of the American Ceramic Society*. 84: 2882-2888.

[27] Deshpande, S. B. Potdar, H. S., Patil, M. M., Deshpande,V. V. and Khollam, Y. B. Khollam (2006). Dielectric Properties of $BaTiO_3$ Ceramics Prepared from Powders with Bimodal Distribution. *J. Ind. Eng. Chem*, 12(4): 584-588.

[28] Uchino, K. Sadanaga, E. Hirose, T. (1989). Dependence of the Crystal Structure on Particle Size in Barium Titanate. *J. Am.Ceram.Soc.*72, 1555–1558

[29] Sagar, R. Hudge, P. Madolappa, S. Kumbharkhane, A.C. Raibagkar, R.L. (2012). Electrical properties and microwave dielectric behavior of holmium substituted barium zirconium titanate ceramics. *Journal of Alloys and Compound*. 537, 197

[30] Plocharski J, and Wieczoreck W. PEO based composite solid electrolyte containing NASICON. Solid State Ionics 1988; 979: 28-30.

[31] Kumar A, Singh B.P, Choudhary R.N.P, Thakur A. K. Characterization of electrical properties of Pb-modified $BaSnO_3$ using impedance spectroscopy, Materials chemistry and Physics, 2006; 99 (1), 150-159

[32] Yang, C.F. (1996). Improvement of the sintering and dielectric characteristics of surface barrier layer capacitors by CuO addition, *Jpn. J. Appl. Phys.*35, 1806–1813.

[33] Hirose, N., and West, A.R. (1996). Impedance Spectroscopy of Undoped $BaTiO_3$ Ceramics. J. *Am. Ceram. Soc.* 79(6), 1633-1641,

[34] Dutta, A., Bharti, C., Sinha, T.P. (2008). AC Conductivity and Dielectric Relaxation in $CaMg_{1/3}Nb_{2/3}O_3$," *Materials Research Bulletin*, 43(5), 1246-1254. doi:10.1016/j.materresbull.2007.05.023

[35] Ganguly, P., Jha, A. K., Deori, K. L. (2008). Complex impedance studies of tungsten–bronze structured $Ba_5SmTi_3Nb_7O_{30}$ ferroelectric ceramics, *Solid State Communications*, 2008; 146 (11-12), 472-477

[36] Ranjan, R., Kumar, N., Behera, B., Choudhary, R. N. P. (2014). Investigations of Impedance and Electric Modulus Properties of $Pb_{1-x}Sm_x$ $(Zr_{0.45}T_{i0.55})_{1x/4}O_3$ ceramics. *Advanced Materials Letters*, 2014; 5 (3), 138-142.

[37] Morrison, F.D., Sinclair, D.C., West, A.R. (2001). Characterization of lanthanum doped barium titanate ceramics using impedance spectroscopy. *J. Am. Ceram. Soc.* 84, 531–538.

[38] Sen, S., Pramanik, P., Choudhary, R.N.P. (2007). Effect of Ca-additions on structural and electrical properties of Pb (SnTi) O3 nano-ceramics. *Ceram. Int.* 33(4), 579-587.

[39] Behera, B., Nayak, P., Choudhary, R.N.P. (2007). Study of complex impedance spectroscopic properties of $LiBa_2Nb_5O_{15}$ ceramics. *Materials Chemistry and Physics,* 106 (2-3), 193-197.

[40] Das, P.S. Chakraborty, P.K. Behera, B. Choudhary, R.N.P. (2007). Electrical properties of $Li_2BiV_5O_{15}$ ceramics. *Phys. B* 395, 98D, doi: 10.1016/j.physb.2007.02.065

[41] Behera, B., Nayak, P., Choudhary, R.N.P. (2008). "Structural and impedance properties of $KBa_2V_5O_{15}$ ceramics", *Mater. Res. Bull.,* 43, 401–410.

[42] Saha, S. and Sinha, T.P. (2002). "Low-temperature scaling behavior of $BaFe_{0.5}Nb_{0.5}O_3$". *Phys. Rev. B*, 65, 13410

[43] Jonscher, A.K. (1977). The 'universal' dielectric response. *Nature* 267, 673-679

[44] Rivera, I., Kumar, A. Ortega, N. R. Katiyar, S., Lushnikov, S. (2009). "Divide line between relaxor, di□used ferroelectric, ferroelectric and dielectric", *Solid State Commun.*, 149 [3-4]172–176.

[45] Khalid, S., Ikram, M. and Asokan, K. (2014). Structural, optical and dielectric study of Mn doped $PrFeO_3$ ceramics. *Vacuum* 99, 251-258. https://doi.org/10.1016/j.vacuum.2013.06.014